

# Asymmetric Skin Lesion Instance Detection And Foreground Patch Uprooting Based On Dseg-Net

Gopikha S<sup>1</sup> and Balamurugan M<sup>2</sup>

<sup>1,2</sup> School of Computer Science and Engineering,  
Bharathidasan University, India.

---

## Abstract

Melanoma is the most lethal malignant neoplasm, and it's becoming more common. Early control and mitigation of skin cancer can optimise a person's chance of survival. Due to the prevalence of distracting factors such as lighting fluctuations and light reflections off the skin surface, studying these dermoscopic images can indeed be difficult for dermatologists. The precise demarcation of the skin pathology area is critical in determining the type of skin illness. This paper proposed a method, named DSeg-net, for patch detection and uprooting of pigmented skin lesions. This method combines deep convolutional neural networks, termed YOLOv5, for patch detection, asymmetric patch contouring for edge preservation, and clustering techniques to determine pixel groups for patch uprooting. Hairs in the input images of ISIC-2018 and 2019 challenging dataset are removed using De Trop Noise Exclusion with in-painting, and additionally, all the skin images with multiple sizes and shapes of lesions are meticulously annotated with rectangle bounding, and yolov5 hyper- parameters have been tuned to detect multiple lesions in the dermoscopic images with a high confidence score. Even in the midst of fuzz bounds and complicated textures, our technique can reliably detect and label patches while also accurately segmenting the skin pathology areas. On these two datasets, the proposed model's efficiency is evaluated using various parameter measures. The results proved that the proposed segmentation techniques achieved nearly 92% to 94% of overall average accuracy on two different datasets.

**Keywords:** Melanoma; YOLOV5 Detection; Image Annotation; Clustering; Skin Lesion Patch Uprooting.

## 1.Introduction

Nowadays, the total of melanoma patients affected by high global warming has dramatically increased. Melanoma is the most dangerous and severe skin disease that frequently begins in skin pigment cells with malignant tumors. According to a study, more than 70 percent of the fatalities of individuals with skin cancer are caused by malignant melanoma tumors [1, 2]. Melanoma is one of the most common skin conditions with a significant fatality rate [3]. In melanoma, the survival percentage is considerably higher if identified early. Skin cancer melanoma can distress the liver, the bones, the lungs, and the cerebrum if it is not recognized

in initial times and is very difficult to identify. The melanoma is commonly evaluated with the use of clinical camerawork for the initial clinical evaluation. The technique of dermoscopy is often used for assessing lesions of melanoma as a technique for non-invasive image analysis [4]. Dermoscopy is used to identify patterns of melanoma lesions in melanoma skin lesions. The vascular components of skin lesions can also be diagnosed with this method[5]. The instrument used to diagnose vascular components is called a dermoscope, which represents an overall microscope of more than 10 times significant lens quality and magnification quality. Most recent dermoscopic images, however, are manually evaluated by dermatologists and are time intense, exclusive and difficult. In the meantime, each individual dermatologist can readily prejudice the diagnostic result. The CAD can tackle these challenges successfully. It not only recovers the revealing efficacy but also contributes to an objective diagnosis. The development of a CAD using melanoma detection scheme is therefore impending and essential [6].

In melanoma of skin, lesion segmentation is most important techniques because lesion segmentation precision impacts diagnostic and classification performance. The loss segmentation procedure, however, is challenging because to its many areas with lesions, lesion structures, fluctuating boundaries, multiple colors of the skin and complex backdrop areas[7]. The weak contrast in the photograph also resulted from discriminating towards the neighboring tissue cells. Further restrictions such as hair, ebony frame, ruler's mark, blood vessel, and color lighting all make it much more difficult to segment skin injury images[7]. In addition, lesions are identified and separated from the surrounding environment utilizing the segmentation technique for skin lesions for dermoscopic pictures. Extra products such as hair and reflections complicate segmentation. The segmentation of images is used to separate an image into its main parts. Image segmentation stated as the way the required area is segmented. The major segmentation goal is the division of a high correlation image and region of interest (ROI). ROI extraction is the most crucial phases following preprocessing in skin lesion dermoscopic images[9-10].

The skin cancer tumor is typically seen in moles. The perimeter, color, symmetry and mole design and borders of the tumor can be detected. The precision of segmentation is therefore highly important since it mainly influences the detection of skin lesions. Several researchers have demonstrated an interest in efficient melanoma segmentation and huge amounts of diagnosis of melanoma have been carried out in early stages[11-12]. Various academics are therefore presenting numerous existing techniques, particularly k-mean algorithms, CAD methods, saliency, convolution and disconvolution networks, and fuzzy algorithms. Although these technologies have been quite successful, the task of segmentation of the skin cancer remains challenging. First of all, images of a dermoscopy may comprise hair, blood vessels and other segmentation-interfering components. In addition, the low contrast among the lesion region and the skin around it generates the blurred border, making it problematic to precisely segment the lesion. Finally, melanoma frequently has diverse sizes, forms and colours, contingent on different skin conditions, which could be an obstacle to a high level of segmentation. Existing dermoscopic skin lesion segmentation systems are mostly computationally costly and imprecise[13]. This paper presents Dseg-Net, an optimal pipeline for segmenting skin cancer lesions that incorporates a combination of YOLOV5 and clustering

algorithms. Multiple strategies are used in this work for accurate patch detection and uprooting: The first stage is to directly attribute a denoised image; the second step is to manage image annotation for all skin images. To detect images and patches, the YOLOV5 network is employed. The third stretch entails determining whether a detected patch is ready for grayscale processing. The thresholding process is the fourth phase. Contours execute asymmetric patch instance detection using the binary image as a feed in the fifth phase. The final stage is to discover and cluster diverse asymmetric patches, and then foreground them. The validation of these strategies is done utilizing two independent metric data sets. The remainder of the paper is organized: Section 2 discusses the associated work of existing skin cancer segmentation approaches. Section 3 offers the thorough explanation of the suggested segmentation process. Section 4 provides the experimental validation of the projected methodology using existing segmentation measures. Finally, Section 5 presents the conclusion of the research with its future work.

## 2. Related works

In 2018, Al-Masni et al. introduced a novel approach to the segmentation of skin lesions dubbed a Full-Resolution Recovery Network (FrCN)[14]. The benefit of this model is that subsampling layers are eliminated and full architectural resolution is used throughout the training. This allows you to simply retrieve the needed precise characteristics from the input image. They assessed their profound classical on two datasets, PH2 and ISBI 2017. The test results on the sensitivity, specialty, accuracy on the 2017 ISBI dataset be present 85.40%, 96.69%, 94.03%, and 93.72%, 95.65%, respectively. 95.08% on the PH2 dataset. However, patch detection is not carried out in this work for effective segmentation.

In 2018, Hang Li et al. distributed a deep model for the segmentation of skin lesions, called a Dense Deconvolutional Network (DNN). They have dense devolutionary layers (DDL), residual chained pooling (CRP) and hierarchic monitoring (HS) [15]. DDL has been trained to retain the same input and output image resolution without previous knowledge and expensive post-processing techniques. They employed CRP to extract rich contextual information by using a combination of local and global contextual characteristics and HS as a loss assistant to recover the prediction mask. They employed the 2017 ISBI dataset for their model assessment and gained 0,866%, 0,765% and 0,939% of the findings, respectively, for the Dice coefficient, the Jaccard index (JI), accuracy. The JI is very low due to more number of layers used in DNN network.

In 2018, Peng used an adversarial network segmentation design. They used the GAN to help segment skin lesions[16]. They employed a U- network as a generator and a CNN network as a discrimination against the basic reality and the mask. They assessed their ideal on the 2016 ISBI and attained an usual segmentation accuracy of 0.97% and the Dice coefficient of 0.94%. Yuan et al. recently suggested a method of segmentation in 2019 [17]. They have constructed a deeper network construction with 29 layers and used small kernel filters in order to achieve more detailed characteristics and increase their architecture's discrimination. They examined their strategy with the 2017 ISBI data set and reached the Jaccard index rate of 0.76 percent. But, these methods needs effective clustering model for accurate segmentation.

In 2017, Ahn, et al. [18], lesion segmentation using saliency detection approaches is presented to rebuild errors that can be better and separate from the surrounding areas, deriving from the ideal of sparse representation combined with a backdrop detection. The Author Zamani Tajeddin[19] presented in 2016 the categorization of patients with melanoma which can be accomplished using the characteristics retrieved using DLM, diagnostic performance is considerably increased by the separation of the lesions. Both publications used the ISIC validation procedure data set. The methods can't handle the fuzz bounds and complicated textures.

The author Bozorgtabar [20] proposed a skin lesion segmentation approach for dermoscopic images in 2016 by using the skin image context information on a superpixel level. In specifically, a sparse coding from Laplacian is provided to assess the probability of skin pixels for delineating lesion frontiers. In addition, as the lesion segmentation process, a new regulatory smoothing technique is proposed. But, the skin image is multi-scale superpixel segmented that are difficult to manage the size variations of the identified border.

In 2017, H. Zhao developed another approach in the field of deep segmentation, i.e. the Pyramid scene parsing network (PSPN) [21] that analyzes the melanoma lesion environment and extracts deep interested fields to acquire the melanoma at the global level. In 2017, Chen[22] created a DeepLab model which is employed for the segmentation of the melanoma in atrocious convolutions and atrocious spatial pyramid pooling. The DeepLab model extracts the backbone ResNet101 and atrocious convolution features to alter the dermoscopic picture with the equal resolution as the input image. DeepLab's ASPP network classifies melanoma lesion at a pixel level. The segmentation findings for PSPN and DeepLab V3 are equivalent to the suggested YOLO V4 model with active melanoma contour segmentation. But, edge perservation is not done by these techniques.

TPH-YOLOv5 was proposed by Zhu et al. [23]. Using YOLOv5, add a sixth prediction head to account for things of varying scales. With Transformer Prediction Heads (TPHs), we'll look at the prediction potential with a self-attention mechanism instead of traditional prediction heads. Include a convolutional block attention model (CBAM) for locating the attention zone in scenes with packed items. Our suggested TPH-YOLOv5 can benefit from a variety of approaches, such as data augmentation, model integration, and the introduction of an additional classifier, which we discuss in detail below. TPH-YOLOv5 has shown good performance and impressive interpretability on drone-captured situations in extensive investigations on the dataset VisDrone2021. While training and testing are in a small range, the AP result of TPH-YOLOv5 on DET-test-challenge dataset is 39.18 percent.

Skin lesion classification using mutual bootstrapping deep CNN(MB-DCNN) models have been anticipated by Xie et al. [24]. We've built this model with a segmentation network, a mask guided classification network, and an upgraded segmentation layer on top of the whole thing. While on the one hand, the coarse-SN constructs coarse lesion masks to aid the mask-CN in finding and accurately classifying skin lesions, the fine-SN does the opposite. Mask-CN creates lesion localization maps, which are subsequently fed into enhancedSN for accurate lesion segmentation using the localization information learnt by mask-CN. Using this

technique, segmentation networks share and support classification networks by bootstrapping their knowledge. By using a unique rank loss in combination with a Dice loss to compensate for class imbalance and hard-easy pixel imbalance, we are able to overcome these issues. With the use of the ISIC-2017 and PH2 datasets, we investigate the suggested MB-DCNN model and achieve a Jaccard index of 80.4% and an AUC of 93.8% and 97.7% for skin lesion segmentation and grouping, respectively. But, it's necessary to improve the discriminatory ability of bootstrapping characteristics.

In a study by Hasan et al. [25], they proposed the Dermoscopic Skin Network, a novel and automated semantic segmentation network for detecting skin lesions (DSNet). To decrease the amount of parameters and lighten the network, employed a depth-wise separable convolution instead of a standard convolution to project the learnt discriminating features onto the pixel space throughout the encoder, also, built a U-Net and a Fully conv layer. In to test the proposed DSNet (FCN8s). This model is evaluated and improved on the basis of two freely available datasets: ISIC-2017 and PH2. The mean intersection over union (mIoU) for the ISIC-2017 and PH2 datasets was 77.5 percent and 87.0 percent, respectively, exceeding the mIoU of the ISIC-2017 challenge winner by 1.0 percent. Additionally, the network beat U-Net and FCN8s on the ISIC-2017 dataset by 3.6% and 6.8%, respectively.

In order to deal with uncontrolled psoriasis photos for CAD, Lin et al. [26] have described an excellent solution based on deep convolutional neural networks for instance segmentation. If you'd like to achieve instance segmentation for psoriasis photos, use the YOLACT network made up of a backbone and a FPN, Protonet and a prediction head. Image feature extraction is done via the backbone network and FPN is designed to build multiscale feature maps for accurately classifying and locating objects of various sizes. The YOLACT++ model is retrained using transfer learning to attain instance segmentation for unconstrained psoriasis pictures. Following cross validation, the suggested system's mAP rates were at least 85.9%. In terms of efficiency, the proposed technique's FPS rate reached 15 frames per second. However, a variety of unrestricted psoriasis photos with varied degrees of severity is not tested in this work.

An early stage skin lesion localization, segmentation, and categorization system was developed by Anjum et al. [27]. There are three stages to the strategy that has been proposed. Open neural networks (ONNX) and squeeze net models serve as a backbone for the tinyYOLOv2 model, which is used in phase I to locate various forms of skin lesions. The features are obtained from the squeezing net's depthconcat7 layer and sent to tinyYOLOv2. The proposed model is capable of pinpointing the exact location of the skin injury. Segmentation is performed in Phase II using a 13-layer 3D-semantic segmentation model (01) input (4 convolutions), 3 batch normalization (3 ReLU layers), softmax (3 layers), and pixel classification (3 layers). The overlap zone among the segmented and ground truth images is computed using a pixel classification layer in the proposed segmentation model. In Phase III, deep features will be extracted with the ResNet-18 model and optimum features will be selected with the ant colony optimization (ACO) approach. Classifiers like optimized (O)-SVM and O-NB use the features vector supplied by the classifiers with optimized (O). The suggested

method is tested on the most demanding MICCAI ISIC datasets from 2017 to 2019. With the help of ISBI 2017 and ISIC 2020 datasets, a mAP of 0.95 was produced. However, the method is failed to to detect multiple lesions in the dermoscopic images.

With the most discriminating deep features, Khan et al. [28] offer a completely automated approach for multiclass skin lesion classification. To begin, photos are enhanced using color-controlled local histogram intensity values (LCcHIV). Using a ten-layer proprietary CNN, we estimate saliency using a novel Deep Saliency Segmentation approach. A thresholding function transforms the resulting heat map into a binary image for use in other software applications.. After that, a deep pre-trained CNN model extracts features from the segmented color lesion images. We implement an upgraded moth flame optimization (IMFO) approach to pick the most discriminant features to overcome the curse of dimensionality. The resulting characteristics are combined with the help of a multi-set maximum correlation analysis (MMCA) and then classified using the Kernel Extreme Learning Machine (KELM) classifier. The suggested methodology achieves segmentation accuracy of 95.38%, 95.79%, 92.69%, and 987.0%, respectively. It was found that the classification performance was 90.67 percent accurate when tested on the HAM10000 data set. For effective analysis, pixels are not clustering in this work.

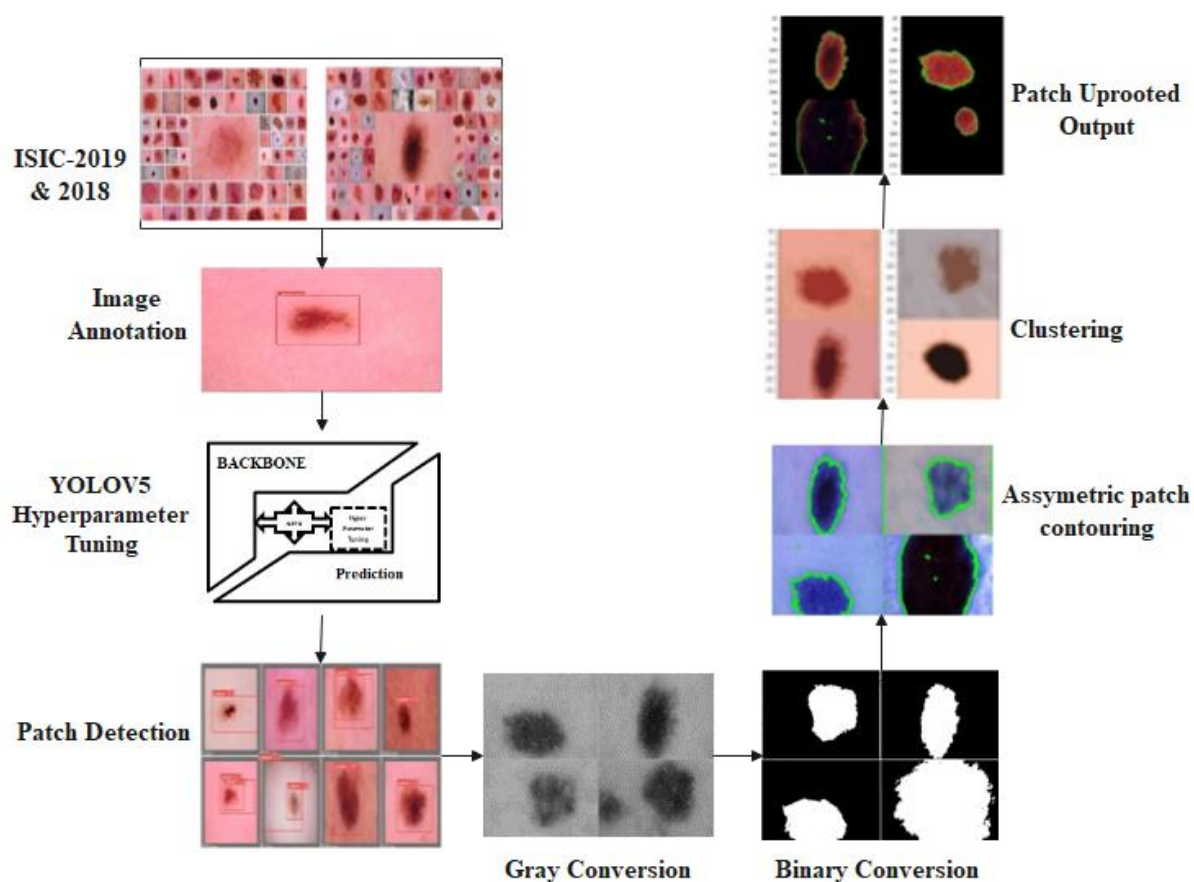
A new CNN design based on auxiliary information has been developed by Liu et al. [29]. Segmentation and edge prediction are both being done at the same time. When the proposed cross-connection layer module is used, it feeds the in-between feature maps from one job into a neural network's boundary area, causing the neural network to focus on that boundary region implicitly. With a Jaccard Index of 79.46 %, an Accuracy of 94.32 %, and a Sensitivity of 88.76 %, this method exceeds existing state-of-the-the-art methods. But, rectangle bounding technique is used to detect the multiple sizes and shapes of lesions.

New YOLO approaches to object detection have been put out by Redmon et al., [30]. The bounding boxes and class probabilities are predicted by a single neural network directly from entire images in a single assessment. Using a single network to monitor the entire detection procedure allows it to be tuned for best results. Our unified architecture is lightning fast because to the optimizations we've implemented. A 45-frames-per-second real-time YOLO model is used as the foundation for more advanced models. YOLO's Fast YOLO network processes 155 frames per second, which is amazing when compared to other real-time detectors' mAP. YOLO makes more localization errors but is less likely to forecast false positives on the backdrop when compared to current detection techniques.

### **3. Proposed System**

In this section, the five different methodologies for segmenting the input data are explained briefly. Figure 1 displays the working procedure of the projected research work. Initially, the input image is taken from two challenging datasets, where patch detection is occurs by using YOLOv5 network. The output of this network will given as an input for gray conversion technique (i.e.colour images are converted into gray scale images). The binary mask creation is done by using OTSU thresholding technique, where the edges of the images are preserved

by using Assymmetric patch Contouring technique. In order to identify the pixel groups, this research work uses the Patch detection based k-means clustering technique. Finally, the segmented output of skin cancer lesion is achieved.



**Figure.1.** Proposed Flow Diagram.

### 3.1. Input Image

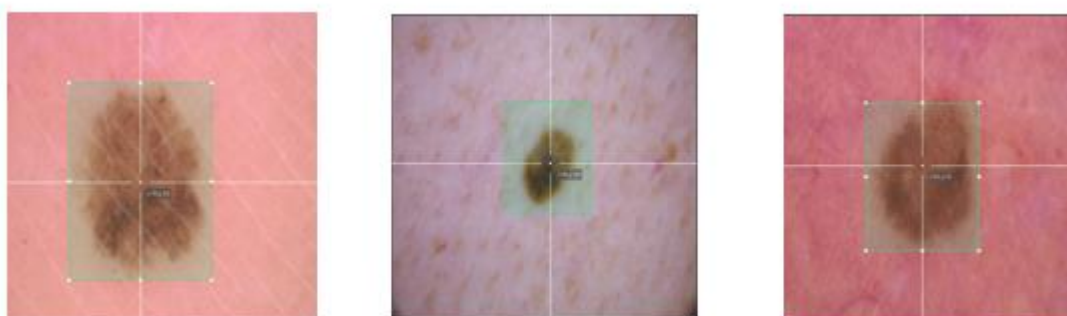
Initially, the input image is collected from the 2019 and 2018 ISIC challenging datasets. Vintage boosting, grey contrast stretching, filtering, mask construction, and DeTrop Noise Exclusion using in-painting are five procedures outlined in the proposed research to eliminate the hair from the input images. This technique aids in the separation of the relevant component from the backdrop and the extraction of information from pixels of similar classes in the immediate vicinity. Following this procedure, the output images are used as input images in our proposed approach. Figure 2 shows some samples of images.



**Figure 2:** Sample Input images.

### 3.2. Image Annotations

Image annotation is the primary process of labelling images of a dataset to train the DL model. Annotating pigmented skin cancer images can help in identifying the features of the lesion and sensing the sum of lesion patches existing in the image, even if the lesion is of different sizes and forms. The python script was used to build rectangle bounding boxes over the affected area of skin patches and lesions, and the object was annotated as Lesion. Dermoscopic images can contain two or more lesion in some circumstances. Figure 3 shows the sample bounding box images.



**Figure 3:** Sample images for bounding box.

The labelling for one row per object is described as:

- Each row is labelled with x\_center, y\_center, width, and height.
- Class records are zero-indexed (they begin with 0).

The following Table 1 shows the sample labels values

**Table 1:** Samples labels

class	X center	Y center	width	height
0	0.505945	0.480185	0.894320	0.910172
0	0.548877	0.579260	0.549538	0.540291

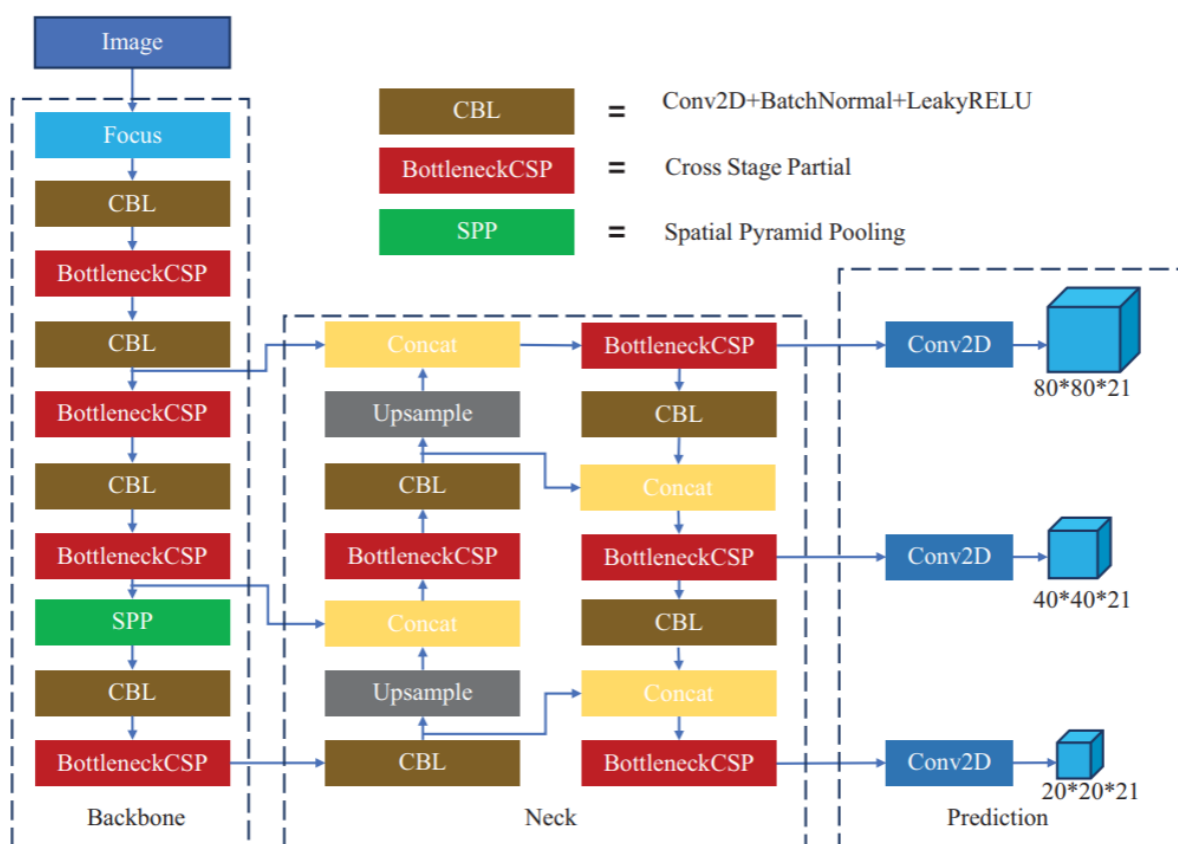
### 3.3. YOLOv5 and Patch Detection

This network is used to identify patches here. As illustrated in Fig. 4, the YOLOv5 [31-32] network structure is separated into three components, backbone, neck and output. In the backbone, the input picture with a resolution of 640 bis640 alias 3 passes by the Focus structure. Following the slicing procedure, it first becomes a 320 GPM feature map, then a 3 20 GPM feature map and then a 320 GPM feature map after the convolution of three-two kernels. The



CBL module is a basic module for convolution. Conv2D + Batch Normal + Leaky RELU is a CBL module.

The Bottleneck CSP module mainly extracts features in the feature map and extracts rich picture information. Compared to other big convolutionary neural networks, the structure of the Bottleneck CSP can minimise the gradient information duplication in the process of optimisation of convolutionary neural networks. Its parameter quantity occupies the majority of the whole network parameter quantity. Four variants with various characteristics, namely YOLOv5, YOLOv5m, YOLOv5l and YOLOv5x, can be obtained by setting the width and depth of the Bottleneck CSP module. The SPP module essentially boosts the network's receptiveness and acquires distinct scale properties.



**Figure 4.** YOLOv5 network structure.

YOLOv5 additionally adds a pyramid structure based on the FPN framework. The FPN layer sends strong semantical features from upper to lower using this combination operation, and the feature pyramid transmits robust placement from the bottom up. Combine feature aggregation from multiple layers in instruction to progress the ability of the network to recognize different size objectives.

Before running Yolov5, all the obtained datasets were resized to 224\*224 resolution for training and validation. The images in the training and validation sets were then annotated and bound to form a rectangle box over the skin lesion. The focus is on the confined rectangular area, which is referred to as the foreground. Dermoscopic images of an extensive variety of

lesions and patches are bound and annotated as lesions. There are three processes in YOLOv5: bounding box, annotation, and confidence score [33].

Trust is the increase in the possibility of the existing element and the union intersection (IoUs) % as shown below:

$$\text{Confidence} = \text{Pr}(\text{object}) * \text{IoU}_{\text{predicted}}^{\text{Ground Truth}} \quad (1)$$

If the associated cell does not have an item, the confidence score must be 0. Otherwise, the trust value is the same as the IoU. Each bounding box has 5 variables like x, y, w, h, and a confidence score. x and y denote co-ordinates of the bounding box central point whereas w and h reflect values of width and height. An additional C variable is also available for the class scores. C conditional class probabilities  $\text{Pr}(\text{Class}_i|\text{Object})$  is forecast by every grid cell. By multiplying the conditional class probabilities and forecasts of particular cases, YOLO creates class-specific confidence values for each box, as indicated in Formulation 2. These scores show the probability that this class is found in the box and how well the finally decides matches the object

$$\text{Pr}(\text{Class}_i|\text{Object}) * \text{Pr}(\text{Object}) * \text{IoU}_{\text{predicted}}^{\text{Ground Truth}} = \text{Pr}(\text{Class}_i) * \text{IoU}_{\text{predicted}}^{\text{Ground Truth}} \quad (2)$$

The foreground bounding box information and concern labels for the images are demanded by YOLOv5. The YOLO format has been used to export the annotated set. The IoU threshold is set to 0.35 and the confidence score is set to 0.65. For skin patch detection, the YOLOv5s cfg is employed. The model has undergone training with 25-epoch is used to train the model. The momentum hyperparameters are set to 0.945. At the end, output the detected results and object coordinates, where the sample output images are shown in Figure 5. An accuracy of 97% to 91% is achieved in detecting the lesion by using this patch detection technique. The accuracy graph is depicted in the figure 6 and 7.



**Figure 5.** Sample YOLOv5 Applied images

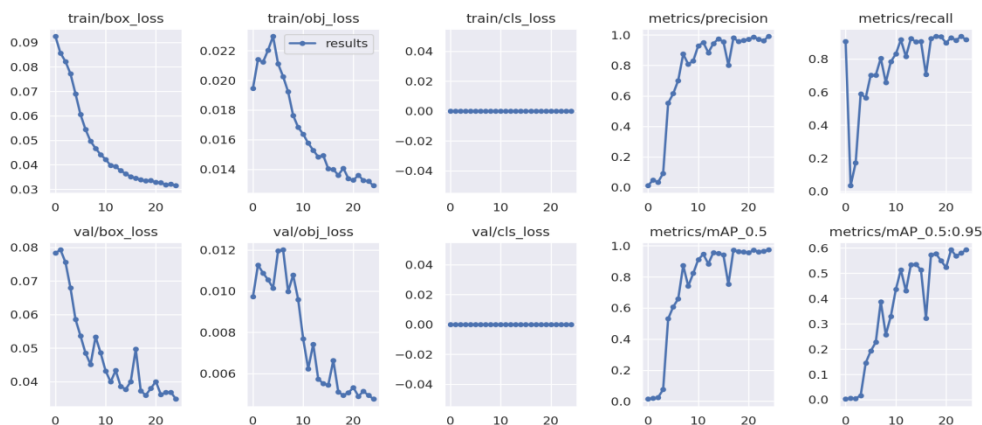


Figure 6: Results of Patch Detection technique that achieved 97% of accuracy.

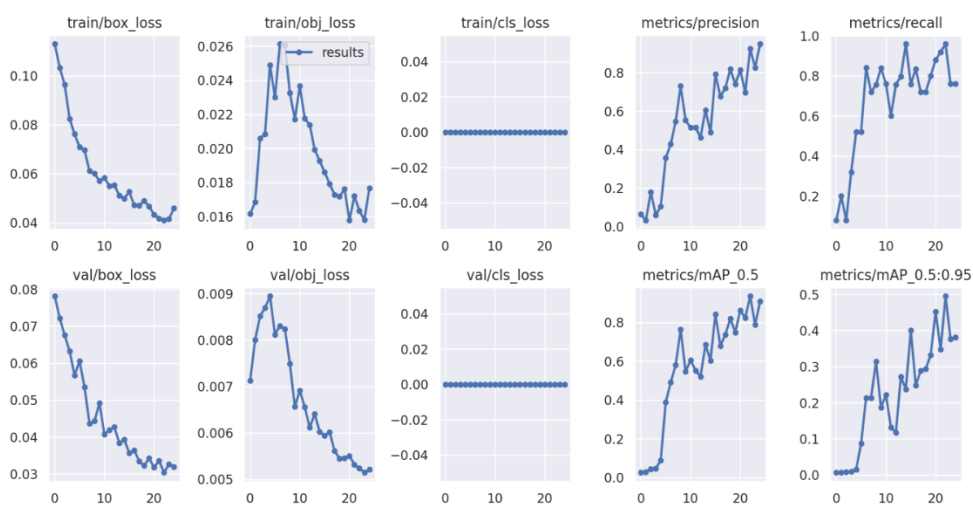


Figure 7: Results of Patch Detection technique that achieved 91% of accuracy.

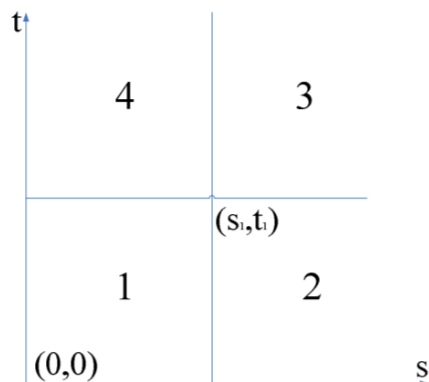
### 3.4. Two-Dimensional Otsu Algorithm

After the patch detection, the color image is converted into gray scale images by using gray conversion technique. If the gray level of an image is  $L$ , the gray level of its pixels for the neighborhood is similarly  $L$ . Therefore, the grayscale value  $I$  of each pixel and its average neighborhood grayscale value  $j$  are two-dimensional  $(i, j)$ . Suppose the time of array  $(i, j)$  is  $f_{ij}$ ,  $N$  is the total pixel number, the two-dimensional density function is the

$$P_{i,j} = \frac{f_{ij}}{N} \quad (3)$$

And it satisfied the function:  $\sum_{i=0}^{L-1} \sum_{j=0}^{L-1} P_{i,j} = 1, N = \sum_{i=0}^{L-1} \sum_{j=0}^{L-1} f_{i,j}$

Assume that the pixels are  $C_0$  and  $C_1$ , the threshold is  $(s,t)$ , the two-dimensional histogram threshold is separated into four portions, as seen in figure 8.



**Figure 8.** 2D Histogram.

Here, when the position is distant from the diagonal, we suppose  $P_{i,j} = 0$ . In other words,  $C_0$  and  $C_1$  are in the first and third histogram field

So, their probabilities are respectively:

$$\omega_0 = \sum_{i=0}^s \sum_{j=0}^t P_{i,j} \quad (4)$$

$$\omega_1 = \sum_{i=s+1}^{L-1} \sum_{j=t+1}^{L-1} P_{i,j} \quad (5)$$

The mean vectors of  $C_0$  and  $C_1$  are respectively:

$$\mu_0 = (\mu_{0i}, \mu_{0j})^T = \left( \sum_{i=0}^s \sum_{j=0}^t \frac{iP_{i,j}}{\omega_0}, \sum_{i=0}^s \sum_{j=0}^t \frac{jP_{i,j}}{\omega_0} \right)^T \quad (6)$$

$$\mu_1 = (\mu_{1i}, \mu_{1j})^T = \left( \sum_{i=s+1}^{L-1} \sum_{j=t+1}^{L-1} \frac{iP_{i,j}}{\omega_1}, \sum_{i=s+1}^{L-1} \sum_{j=t+1}^{L-1} \frac{jP_{i,j}}{\omega_1} \right)^T \quad (7)$$

Global mean vector is:

$$\mu = ((\mu_i, \mu_j))^T = \left( \sum_{i=0}^{L-1} \sum_{j=0}^{L-1} iP_{i,j}, \sum_{i=0}^{L-1} \sum_{j=0}^{L-1} jP_{i,j} \right)^T \quad (8)$$

Defines the measurement of threshold selection criterion according to the assumption:

$$\begin{aligned} \sigma(s, t) &= \omega_0(\mu_0 - \mu)^T(\mu_0 - \mu) + \omega_1(\mu_{0i} - \mu)^T(\mu_1 - \mu) \\ &= \omega_0(\mu_{0i} - \mu_i, \mu_{0j} - \mu_j)(\mu_{0i} - \mu_i, \mu_{0j} - \mu_j)^T \\ &\quad + \omega_1(\mu_{0i} - \mu_i, \mu_{1j} - \mu_j)(\mu_{1i} - \mu_i, \mu_{1j} - \mu_j)^T \\ &= \omega_0 \left[ (\mu_{0i} - \mu_i)^2 + (\mu_{0j} - \mu_j)^2 \right] + \omega_1 \left[ (\mu_{1i} - \mu_i)^2 + (\mu_{1j} - \mu_j)^2 \right] \quad (9) \end{aligned}$$

So, the best threshold  $(s_1, t_1)$  meet:

$$(s_1, t_1) = \max (\sigma(s, t)) \quad (10)$$

The following figure 9 shows the sample output of OTSU thresholding algorithm.



**Figure 9.** Sample Otsu Algorithm.

### 3.5. Assymmetric Patch Contouring Model

A classic snake is described in the parameters  $X(s) = (x(s), y(s))$ , where  $x(s)$  and  $y(s)$  is  $x$  and  $y$  beside the contour and  $s$  is an arc length with  $[0, 1]$  value to lessen energy function to a minimum.

$$E_{\text{snake}} = \int_0^1 (E_{\text{int}}(X(s)) + E_{\text{ext}}(X(s))) ds \quad (11)$$

Where the first term signifies the internal energy, distinct as

$$E_{\text{int}}(X(s)) = \frac{(\alpha|X_s(s)|^2 + \beta|X_{ss}(s)|^2)}{2} \quad (12)$$

Where  $X_s(s)$  is the chief derivative of  $X(s)$  and  $X_{ss}(s)$  is the following derivative of  $X(s)$  with respect to  $s$ . The exterior energy is distinct as

$$E_{\text{ext}}(X(s)) = -\gamma|\nabla\{G_\sigma(x, y) * f(x, y)\}| \quad (13)$$

Where  $f$  is represented original is image, and  $G_\sigma(x, y)$  is the two-dimensional (2-D) Gaussian kernel with  $\sigma$  as standard deviation. The local minima of  $E_{\text{snake}}$  defined in (11). Based on the Euler-Lagrange attitude, (11) has a minimal when

$$\alpha X_{ss}(s) - \beta X_{ssss}(s) - \nabla E_{\text{ext}}(X(s)) = 0 \quad (14)$$

Where  $X_{ss}(s)$  and  $X_{ssss}(s)$  are the second and fourth outcomes of the curve with deference to the parameter  $s$ .

To invention the solution for (6), the snake is ended dynamic by important  $x$  as the function of time  $t$  and  $s$

$$X_t(s, t) = \alpha X_{ss}(s, t) - \beta X_{ssss}(s, t) - \nabla E_{\text{ext}}(X(s, t)) \quad (15)$$

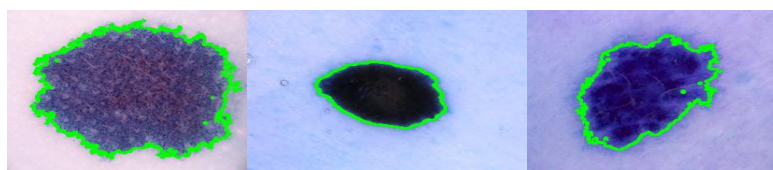
The solution to (15) can be achieved by solving the discrete equations iteratively.

To efficiently lead the snakes into the concave region, in [34] projected a novel external force. Agreeing to the Helmholtz theorem [35], rewriting (15) and swapping the  $-\nabla E_{\text{ext}}(X(s))$  with  $\Theta$ .

$$X_t(s, t) = \alpha X_{ss}(s, t) - \beta X_{ssss}(s, t) + \Theta \quad (16)$$

Where  $\Theta$  is the GVF distinct as  $\Theta(x, y) = [u(x, y), v(x, y)]$  that reduces the energy functional shows in (17), Where  $\nabla\{G_\sigma(x, y) * f(x, y)\}$  is the gradient of the input image  $f(x, y)$  after gaussian smoothing, with variance  $\sigma$  and mean 0. Equation (17) is subjugated by  $u_x^2 + u_y^2 + v_x^2 + v_y^2$  when  $|\nabla\{G_\sigma(x, y) * f(x, y)\}|$  is large, when  $\Theta = \nabla\{G_\sigma(x, y) * f(x, y)\}$ . This result keeps Tim near the gradient of the edge so when snake is close to the object, while permitting the serpent to move to the object, allowing the snake to move to the edge if it is far from the object. The sample preservation of edges using contour model is shown in Figure 10.

$$\Psi = \int \int \mu(u_x^2 + u_y^2 + v_x^2 + v_y^2) dx dy + (|\nabla\{G_\sigma(x, y) * f(x, y)\}|^2 \cdot |\Theta - \nabla\{G_\sigma(x, y) * f(x, y)\}|^2). \quad (17)$$



**Figure 10.** Sample active contour model output image.

### 3.6. Patch Detection based k-means Clustering Algorithm

Clustering is a way of dividing a set of data into a amount of different categories. K-means clustering is one of the prominent methods. In patch detection k-means clustering, it divides the patch collection into a k number of data. It categorizes a given dataset into a distinct cluster number. The k-mean approach based on patch detection contains of two independent steps. In the first stage the centroid k is calculated and in the second phase every point is taken to the cluster with the nearest centroid from the individual data point. There are numerous methods of defining the distance from the nearest center and the euclidean distance is one of the most utilized approaches. Upon grouping, the novel centroid of each cluster will be recalculated and based on this centroid, an each center and data point will be determined and the cluster points with shortest Euclidean distance will be assigned. Each partition cluster is specified by its member and centroid objects. The center of each cluster is to minimize the the items in that cluster. K-means thus is an iterative technique, in which the amount of distances between each item and its center group is minimized across all clusters.

Deliberate an image with a resolution of x digit and the image should be clustered into k cluster numbers. Let  $p(x, y)$  be the cluster input pixels and  $c_k$  be the cluster centres. The algorithm for k-means is as follows

1. Initialize cluster amount k and center. 1.
2. Total the Euclidean distance d among the center and pixel of the picture using the relationship shown below for each pixel of an image.

$$d = ||p(x, y) - c_k|| \quad (18)$$

3. Assign every pixels to the closest center based on distance d.

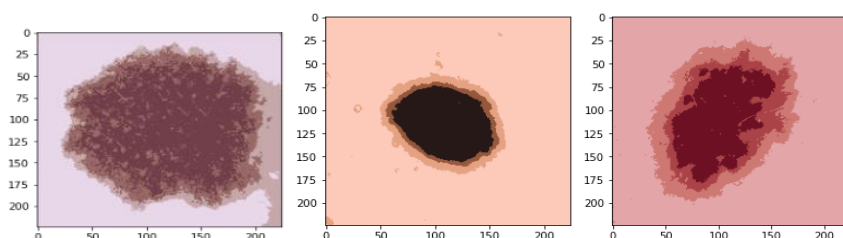
4. Use the following relation to compute the new position of the center after all the pixels have been assigned.

$$c_k = \frac{1}{k} \sum_{y \in c_k} \sum_{x \in c_k} p(x, y) \quad (19)$$

5. Repeat the procedure until the tolerance or error value has been met.

6. Restore the pixel cluster into a picture.

The quality of the outcomes be contingent on the assortment of the initial centroid arbitrarily. If the initial centroid is selected randomly, various results will be achieved for different starting centres. So the starting center is carefully selected so that we are segmented in our desires. And computer complexity is also another term that should be taken into account while creating the K-means cluster. It depends on the amount of data pieces, the amount of clusters and the iteration numeral. The figure 11 shows the sample output images of K-means clustering algorithm.



**Figure 11.** Sample K-means clustering output image.

## 4. Results and Discussion

In this section, the proposed segmentation techniques are compared with existing techniques, which is briefly defined. The section consists of performance metrics, quantitative and qualitative analysis. The proposed system is implemented using Python and Pytorch with 8GB RAM, 1TB hard drive and a 3.0GHz Intel i5 processor. For the proposed results, evaluation ground truth is manually created.

### 4.1. Dataset Description

Here, the two challenging datasets are described as follows:

#### A) ISIC 2019

The dataset is acquired from ISIC (International skin imaging collaboration) 2019 challenge dataset archive which contains benign and malignant skin lesions dermoscopy images. There are 2637 images of training images and 660 testing image.

#### B) ISIC 2018

The dataset is acquired from ISIC (International skin imaging collaboration) 2018 challenge dataset archive which contains benign and malignant skin lesions dermoscopy images. There are 2650 images of training images and 712 testing image.

## 4.2. Performances Metrics

We employ five assessment measures in this study to evaluate the project's performance. We employ the Jaccard Similarity Coefficient (JSC), the Dice similitude coefficient (DSC), precision (ACC), specificity (SPE) and sensitivity using the ISIC 2018 and 19 data sets (SEN). The true positive (TP) rate can be defined for both the ground-reality  $y$  and the forecasted picture  $x$  as a  $TP = y \cap x$ , which is the common area of the segmented area in both  $x$  and  $y$ . The false positive (FP) rate can be described as the  $FP = \bar{y} \cap x$ , which is the segmented non- $y$  area. The False-Negative (FN) rate is specified as  $FN = y$  to be the defective zone in the default image. The true negative (TN) set can be described as  $TN = \bar{y} \cap \bar{x}$ , the backdrop set common both in  $x$  and  $y$ . The true negative (TN) set. We give the following five metrics mathematical expressions: ACC, JSC, DSC, SEN and SPE.

$$ACC = \frac{TP+TN}{TP+TN+FP+FN} \quad (20)$$

$$DSC = \frac{2 \cdot TP}{2 \cdot TP+FP+FN} \quad (21)$$

$$JSC = \frac{TP}{TP+FP+FN} \quad (22)$$


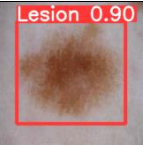
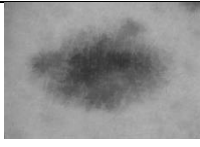
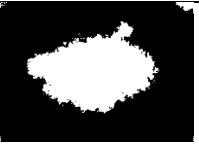
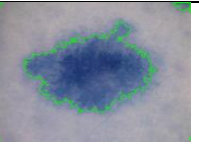
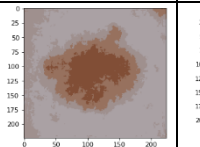
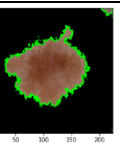

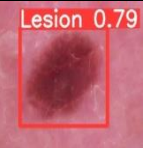
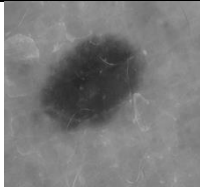
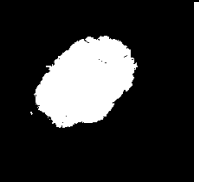
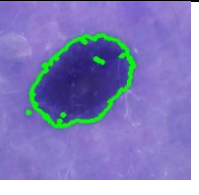
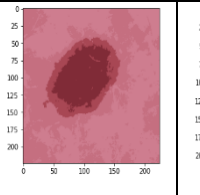
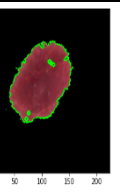
$$SEN = \frac{TP}{TP+FN} \quad (23)$$

$$SPE = \frac{TN}{TP+FP} \quad (24)$$

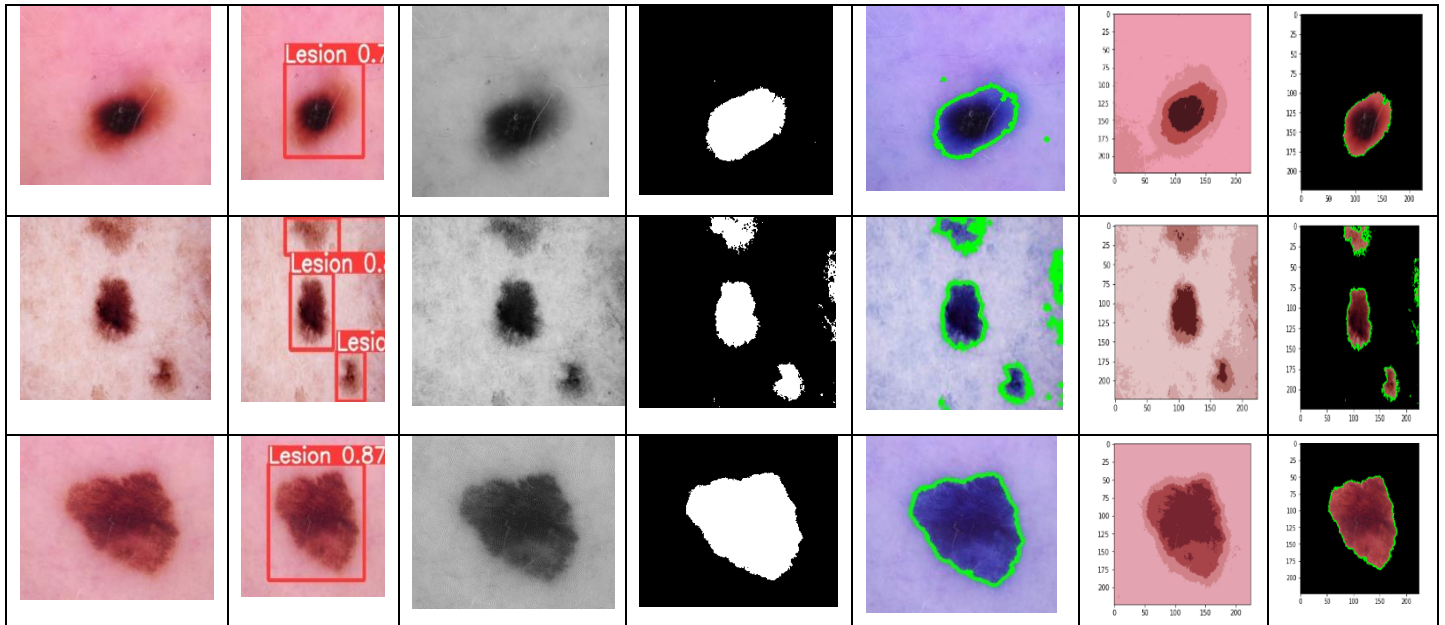
## 4.3. Performance Analysis of Proposed Segmentation Techniques on ISIC-2018

Initially, the output for first five images of ISIC-2018 using different segmentation techniques with final segmented output is provided in Table 2.

**Table 2:** Visual Segmented Output images of ISIC-2018 dataset using different segmentation techniques.

Input Image	Patch Detection using YOLOv5	Gray scale Conversion	Ostu Thresholding	Patch Contouring	K - means Clustering	Patch Uprooted output
						
						

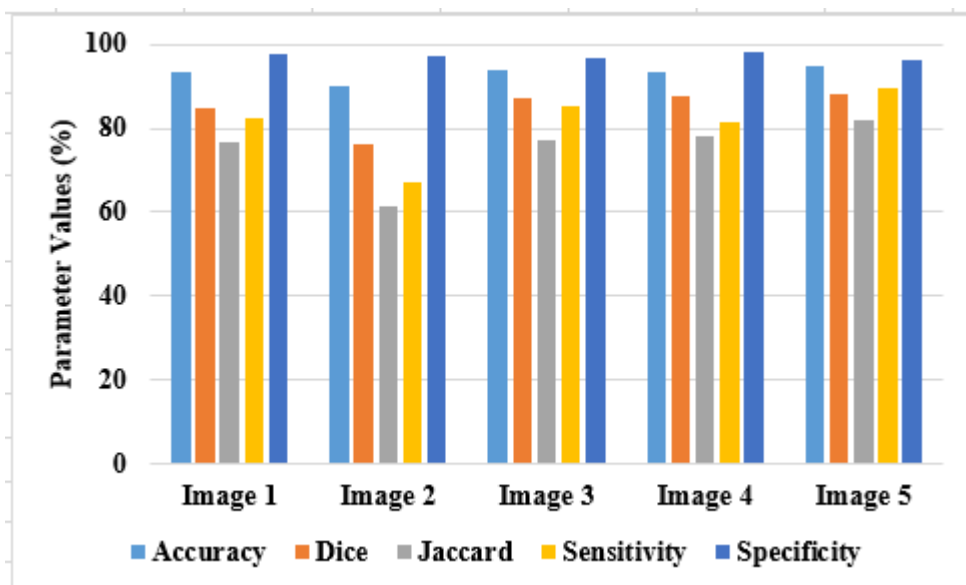




In the next Table 3 and Figure 12 shows the validated results for these five images in terms of ACC, DSC, JSC, SEN and SPE using proposed segmentation technique.

**Table 3:** Experimental Results of Proposed Segmentation technique for the first five images on ISIC-2018 dataset.

Image	Accuracy	Dice	Jaccard	Sensitivity	Specificity
Image 1	93.40	84.90	76.5	82.5	97.5
Image 2	90.14	76.27	61.64	67.15	97.24
Image 3	94.03	87.08	77.11	85.40	96.69
Image 4	93.60	87.80	78.20	81.60	98.30
Image 5	94.70	88.06	82.03	89.80	96.44




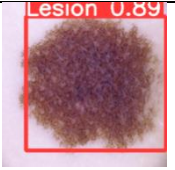
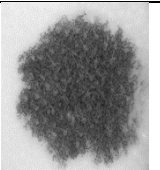
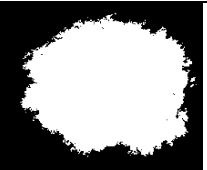
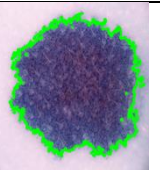
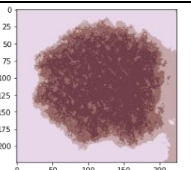
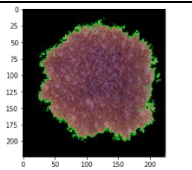

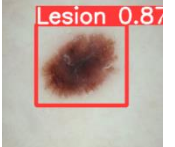
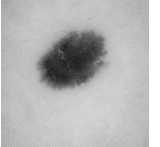

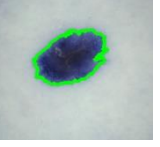
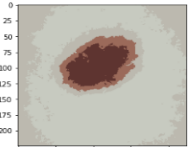
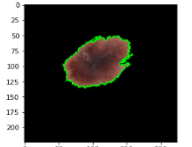


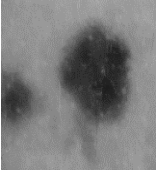
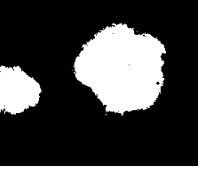
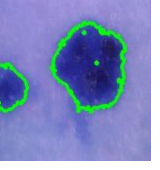
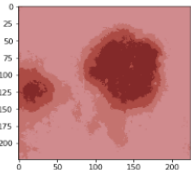
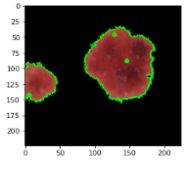

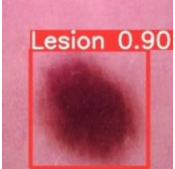
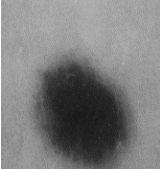

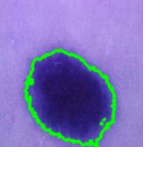
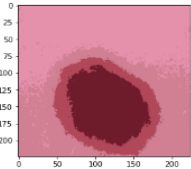
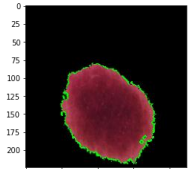

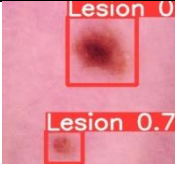
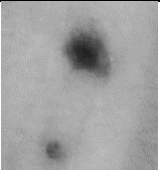
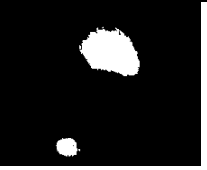
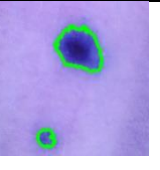
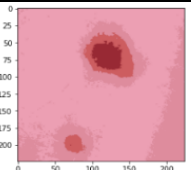
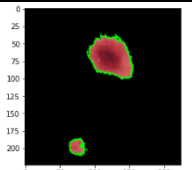
**Figure 12:** Graphical Representation of performance of Proposed Segmentation Technique on ISIC-2018 dataset

For all images, the overall accuracy achieved by proposed segmentation technique is 90% to 94% as well as the specificity achieved by proposed technique is nearly 96% to 98%. When comparing with all images, image 2 achieved less Dice (76%), less Jaccard (61.64%) and less sensitivity (67.15%). Other images achieved nearly 87% of Dice, 76% to 82% of Jaccard and 84% to 89% of sensitivity.

#### 4.4. Performance Analysis of Proposed Segmentation Techniques on ISIC-2019

Initially, the output for first five images of ISIC-2019 using different segmentation methods with final segmented output is provided in Table 4.

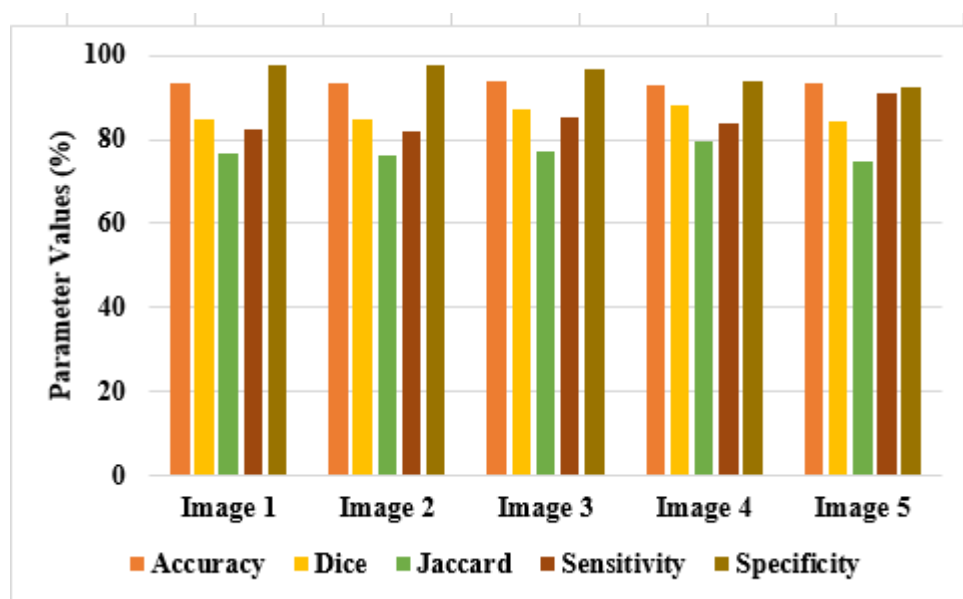
**Table 4:** Visual Segmented Output images of ISIC-2019 dataset using different segmentation techniques.

Input Image	Patch Detection using YOLOv5	Gray scale Conversion	Ostu Thresholding	Patch Contouring	K - means Clustering	Patch Uprooted output
						
						
						
						
						

In the next Table 5 and Figure 13 shows the validated results for these five images in terms of various parameter metrics using proposed segmentation technique.

**Table 5:** Experimental Results of Proposed Segmentation technique for the first five images on ISIC-2019 dataset

Image	Accuracy	Dice	Jaccard	Sensitivity	Specificity
Image 1	93.40	84.90	76.50	82.50	97.50
Image 2	93.20	84.70	76.20	82.00	97.80
Image 3	94.03	87.08	77.11	85.40	96.69
Image 4	92.99	88.13	79.54	83.63	94.02
Image 5	93.39	84.26	74.81	90.82	92.68



**Figure 13:** Graphical Representation of performance of Proposed Segmentation Technique on ISIC-2019 dataset

For all images, the overall accuracy achieved by proposed segmentation technique is 92% to 93% as well as the specificity achieved by proposed technique is nearly 93% to 97%. The accuracy and sensitivity of proposed segmentation technique is low in ISIC-2019 dataset, when compared with ISIC-2018 dataset. All images except image 5 achieved nearly 82% to 85% of sensitivity, where image 5 achieved 90.82% of sensitivity. The Dice of image 1, 2 and 4 achieved only 84%, where image 3 and 5 achieved 88% of dice by using proposed segmentation techniques. In the analysis of Jaccard, all images achieved nearly 75% to 79%, which displays the better enactment of proposed segmentation techniques.

#### 4.4. Comparative analysis

In this section, the performance of projected segmentation method is associated with existing techniques in terms of Dice, accuracy, jaccard and specificity. For the ISIC 2018 dataset for the validation process, as stated in Table 6, current methodologies include [18-22, 28]. Albahli

et al. [28] developed a method of melanoma identification and segmentation which would significantly increase the accuracy of state-of-the-art techniques. As a first phase, artifacts like hair, gel bubbles and clinical marks are removed by morphological procedures and image regions are sharpened from the dermoscopic pictures. The author [28] subsequently employed the YOLOv4 object detector for melanoma detection in order to discriminate strongly associated infected and non-infected regions for the purpose of infected area detection. The melanoma regions are generated by an active contour segmentation method. The infected melanoma patches are extracted. The paper [28] is assessed on ISIC2018 and ISIC2016 data sets for performance evaluation. Therefore, we used the comparison performance only on ISIC2018 dataset.

**Table 6:** Comparative Analysis of Proposed Segmentation Technique with Existing Techniques

<b>Method</b>	<b>Accuracy (%)</b>	<b>Dice (%)</b>	<b>Jaccard (%)</b>	<b>Specificity (%)</b>
Maglogianis [18]	92.8	-	-	97
FAN [19]	93.6	-	-	-
Sparse Coding [20]	91	80	67	86
PSPN [21]	85	86	81	85
DeepLan-v3 [22]	87	85	80	85
YOLOv4-DarkNet [28]	94	-	-	94
<b>Proposed Segmentation Techniques</b>	<b>94.70</b>	<b>88.06</b>	<b>82.03</b>	<b>97.50</b>

From the results analysis, it is clearly proved that the projected segmentation techniques achieved better performance than existing techniques. However, still it requires improvement in Dice and Jaccard coefficient, which can be improved in future work by incorporating efficient feature extraction techniques. The reason for the overall accuracy of 94.70% is that a robust pipeline was followed to segment the lesion in the dermoscopic images in this investigation work by tweaking the hyperparameters of the YOLO network version 5 for patch detection.

## 5. Conclusion

This research discusses Dseg-Net, a new combination segmentation method that employs Yolov5's deep convolutional neural network and clustering techniques. Despite prior deep learning-based segmentation techniques, our methodology uses yolov5 and hyperparameter tuning is done to detect and annotate various lesions in dermoscopic images of diverse sizes

and shapes, as well as varying rectangle bounds to cover vast patches with high detection score. By suppressing the backdrop, the foreground detected region has been zoomed and focussed. Patch uprooting delivers pipeline outcomes by combining many strategies, such as grey conversion, binary mask creation using the OTSU thresholding technique, edge preservation using the asymmetric patch contouring technique, and finally, K-means clustering for pixel group identification. Our proposed scheme efficiently and precisely detects multiple lesions and segments the skin lesions in contrast to state-of-the-art methods. For the ISIC 2018 and the ISIC 2019, we tested our technique using two well-known datasets. The outcomes of this study are optimistic, according to the findings compared to other state-of-the-art methods in terms of accuracy, Dice and SEN in dermoscopy images. Patch detection attains an accuracy of 97% and 91%, respectively. The proposed method attained an overall average accuracy of about 92% to 94%. As an outcome in future work, we will include an DCNN as a feature extraction and classification phase in the pipeline for distinguishing melanoma from segmented skin lesion images.

## References

- [1]. Araújo, R.L., Ricardo de Andrade, L.R., Rodrigues, J.J. and e Silva, R.R., 2021, March. Automatic Segmentation of Melanoma Skin Cancer Using Deep Learning. In 2020 IEEE International Conference on E-health Networking, Application & Services (HEALTHCOM) (pp. 1-6). IEEE.
- [2]. Mane, S. and Shinde, S., 2018, August. A method for melanoma skin cancer detection using dermoscopy images. In 2018 Fourth International Conference on Computing Communication Control and Automation (ICCUBEA) (pp. 1-6). IEEE.
- [3]. Masoud Abdulhamid, I.A., Sahiner, A. and Rahebi, J., 2020. New auxiliary function with properties in nonsmooth global optimization for melanoma skin cancer segmentation. *BioMed research international*, 2020.
- [4]. Alom, M.Z., Aspiras, T., Taha, T.M. and Asari, V.K., 2019. Skin cancer segmentation and classification with NABLA-N and inception recurrent residual convolutional networks. *arXiv preprint arXiv:1904.11126*.
- [5]. Ganesan, P., Vadivel, M., Sivakumar, V.G. and Vasanth, K., 2020, March. Hill climbing optimization and fuzzy C-means clustering for melanoma skin cancer identification and segmentation. In 2020 6th International Conference on Advanced Computing and Communication Systems (ICACCS) (pp. 357-361). IEEE.
- [6]. Zhang, G., Shen, X., Chen, S., Liang, L., Luo, Y., Yu, J. and Lu, J., 2019. DSM: A deep supervised multi-scale network learning for skin cancer segmentation. *IEEE Access*, 7, pp.140936-140945.
- [7]. Araújo, R.L., de Araújo, F.H. and Silva, R.R., 2021. Automatic segmentation of melanoma skin cancer using transfer learning and fine-tuning. *Multimedia Systems*, pp.1-12.
- [8]. Sikkandar, M.Y., Alrasheadi, B.A., Prakash, N.B., Hemalakshmi, G.R., Mohanarathinam, A. and Shankar, K., 2021. Deep learning based an automated skin lesion segmentation and intelligent classification model. *Journal of ambient intelligence and humanized computing*, 12(3), pp.3245-3255.

- [9]. Mohamed, A.A.I., Ali, M.M., Nusrat, K., Rahebi, J., Sayiner, A. and Kandemirli, F., 2017. Melanoma skin cancer segmentation with image region growing based on fuzzy clustering mean. *International Journal of Engineering Innovations and Research*, 6(2), p.91C95.
- [10]. Filali, Y., Abdelouahed, S. and Aarab, A., 2019. An improved segmentation approach for skin lesion classification. *Statistics, Optimization & Information Computing*, 7(2), pp.456-467.
- [11]. Murugan, A., Nair, S.A.H. and Kumar, K.S., 2019. Detection of skin cancer using SVM, random forest and kNN classifiers. *Journal of medical systems*, 43(8), pp.1-9.
- [12]. Lynn, N.C. and Kyu, Z.M., 2017, December. Segmentation and classification of skin cancer melanoma from skin lesion images. In *2017 18th International Conference on Parallel and Distributed Computing, Applications and Technologies (PDCAT)* (pp. 117-122). IEEE.
- [13]. Alquran, H., Qasmieh, I.A., Alqudah, A.M., Alhammouri, S., Alawneh, E., Abughazaleh, A. and Hasayen, F., 2017, October. The melanoma skin cancer detection and classification using support vector machine. In *2017 IEEE Jordan Conference on Applied Electrical Engineering and Computing Technologies (AEECT)* (pp. 1-5). IEEE.
- [14]. Al-Masni, M.A.; Al-Antari, M.A.; Choi, M.-T.; Han, S.-M.; Kim, T.-S. Skin lesion segmentation in dermoscopy images via deep full resolution convolutional networks. *Comput. Methods Programs Biomed.* 2018, 162, 221–231.
- [15]. Li, H.; He, X.; Zhou, F.; Yu, Z.; Ni, D.; Chen, S.; Wang, T.; Lei, B. Dense Deconvolutional Network for Skin Lesion Segmentation. *IEEE J. Biomed. Health Inform.* 2018, 23, 527–537.
- [16]. Peng, Y.; Wang, N.; Wang, Y.; Wang, M. Segmentation of dermoscopy image using adversarial networks. *Multimed. Tools Appl.* 2018, 78, 10965–10981.
- [17]. Yuan, Y.; Lo, Y.C. Improving dermoscopic image segmentation with enhanced convolutional-deconvolutional networks. *IEEE J. Biomed. Health Inform.* 2019, 23, 519–526.
- [18]. Ahn, E., Kim, J., Bi, L., Kumar, A., Li, C., Fulham, M., and Feng, D. D., Saliency-based lesion segmentation via background detection in Dermoscopic images. *IEEE J. Biomed. Heal. Informatics*, p. Accepted to be printed, 2017.
- [19]. ZamaniTajeddin, N. and Mohammadzadeh Asl, B., A general algorithm for automatic lesion segmentation in dermoscopy images. *23rd Iranian Conference on Biomedical Engineering and 2016 1st International Iranian Conference on Biomedical Engineering (ICBME)*. 134–139, 2016.
- [20]. B. Bozorgtabar, M. Abedini, and R. Garnavi, “Sparse coding based skin lesion segmentation using dynamic rule-based refinement,” in *Proc. Int. workshop Mach. Learn. Med. Imag. Athens, Greece: Springer*, 2016, pp. 254–261
- [21]. H. Zhao, J. Shi, X. Qi, X. Wang, and J. Jia, “Pyramid scene parsing network,” in *Proc. IEEE Conf. Comput. Vis. Pattern Recognit. (CVPR)*, Jul. 2017, pp. 2881–2890.

- [22]. L.-C. Chen, G. Papandreou, F. Schroff, and H. Adam, "Rethinking atrous convolution for semantic image segmentation," 2017, arXiv:1706.05587. [Online]. Available: <http://arxiv.org/abs/1706.05587>.
- [23]. Zhu X, Lyu S, Wang X, Zhao Q. TPH-YOLOv5: Improved YOLOv5 Based on Transformer Prediction Head for Object Detection on Drone-captured Scenarios. In Proceedings of the IEEE/CVF International Conference on Computer Vision 2021 (pp. 2778-2788).
- [24]. Xie Y, Zhang J, Xia Y, Shen C. A mutual bootstrapping model for automated skin lesion segmentation and classification. IEEE transactions on medical imaging. 2020 Feb 10;39(7):2482-93.
- [25]. Hasan MK, Dahal L, Samarakoon PN, Tushar FI, Martí R. DS Net: Automatic dermoscopic skin lesion segmentation. Computers in Biology and Medicine. 2020 May 1;120:103738.
- [26]. Lin GS, Lai KT, Syu JM, Lin JY, Chai SK. Instance Segmentation Based on Deep Convolutional Neural Networks and Transfer Learning for Unconstrained Psoriasis Skin Images. Applied Sciences. 2021 Jan;11(7):3155.
- [27]. Anjum MA, Amin J, Sharif M, Khan HU, Malik MS, Kadry S. Deep semantic segmentation and multi-class skin lesion classification based on convolutional neural network. IEEE Access. 2020 Jul 14;8:129668-78.
- [28]. Khan MA, Sharif M, Akram T, Damaševičius R, Maskeliūnas R. Skin lesion segmentation and multiclass classification using deep learning features and improved moth flame optimization. Diagnostics. 2021 May;11(5):811.
- [29]. Liu L, Tsui YY, Mandal M. Skin lesion segmentation using deep learning with auxiliary task. Journal of Imaging. 2021 Apr;7(4):67.
- [30]. Redmon J, Divvala S, Girshick R, Farhadi A. You only look once: Unified, real-time object detection. In Proceedings of the IEEE conference on computer vision and pattern recognition 2016 (pp. 779-788).
- [31]. Github: YOLOV5 <https://github.com/ultralytics/yolov5> & <https://models.roboflow.com/object-detection/efficientdet>.
- [32]. Lin, G.S., Lai, K.T., Syu, J.M., Lin, J.Y. and Chai, S.K., 2021. Instance Segmentation Based on Deep Convolutional Neural Networks and Transfer Learning for Unconstrained Psoriasis Skin Images. Applied Sciences, 11(7), p.3155.
- [33]. Ünver, H.M. and Ayan, E., 2019. Skin lesion segmentation in dermoscopic images with combination of YOLO and grabcut algorithm. Diagnostics, 9(3), p.72.
- [34]. Xu, C. and Prince, J.L., 1998. Generalized gradient vector flow external forces for active contours. Signal processing, 71(2), pp.131-139.
- [35]. Van Bladel, J., 1993. A discussion of Helmholtz' theorem. Electromagnetics, 13(1), pp.95-110.
- [36]. Albahli, S., Nida, N., Irtaza, A., Yousaf, M.H. and Mahmood, M.T., 2020. Melanoma lesion detection and segmentation using YOLOv4-DarkNet and active contour. IEEE Access, 8, pp.198403-198414.